



Optimization of supersonic nozzle flow for titanium dioxide thin-film coating by aerosol deposition

M.W. Lee^a, J.J. Park^a, D.Y. Kim^a, S.S. Yoon^{a,*}, H.Y. Kim^a, D.H. Kim^b, S.C. James^c, S. Chandra^d, Thomas Coyle^d, J.H. Ryu^e, W.H. Yoon^e, D.S. Park^e

^a Department of Mechanical Engineering, Korea University, Seoul 136-713, Republic of Korea

^b Department of Material Science & Engineering, Korea University, Seoul 136-713, Republic of Korea

^c Thermal/Fluid Science & Engineering, Sandia National Laboratories, Livermore, CA, USA

^d Department of Mechanical & Industry Engineering, University of Toronto, Toronto, Ontario, Canada

^e Functional Ceramics Research Group, Korea Institute of Material Science, Changwon, Kyungnam 641-831, Republic of Korea

ARTICLE INFO

Article history:

Received 14 February 2011

Received in revised form

9 July 2011

Accepted 9 July 2011

Available online 22 July 2011

Keywords:

Aerosol deposition

Supersonic nozzle flow

Shockwave

Nozzle optimization

Computational fluid dynamics

ABSTRACT

Aerosol deposition (AD) is an efficient technique for customized coating of various substrates. The small particles of AD yield a dense coating layer with small voids. AD is amenable to rapid coating (mass production), thus, it is economically attractive. Low-temperature AD coating is desirable because it minimizes the thermal degradation of the substrate. An optimized low-cost AD coating technique is of significant interest to solar-cell engineers seeking to reduce manufacturing costs. While most previous studies ignore the importance of nozzle geometry on coating performance, this paper examines non-optimized nozzles and commensurate shockwaves using computational fluid dynamics (CFD). The optimized nozzle geometry obtained from CFD can rapidly prototype nozzles. The CFD-designed nozzles with optimized geometry yielded significantly improved coating quality over non-optimized nozzles.

© 2011 Elsevier Ltd. All rights reserved.

1. Introduction

When conducted at atmospheric pressure, high-speed kinetic coating is referred to as cold spray deposition (Blais et al., 2005; Chun & Ahn, 2011; Fan et al., 2006; Gartner et al., 2006; Jodoin, 2002; Karimi et al., 2006; Katanoda et al., 2007; Li & Li, 2005; Li et al., 2007; Li et al., 2006; Raletz et al., 2006; Zahiri et al., 2009); when conducted in a vacuum environment it is known as aerosol deposition (AD) (Akedo, 2006). Both techniques use high velocity gas jets to accelerated feedstock powders to sufficiently high velocities that high density coatings are produced at temperatures below the melting point of the powder. These are relatively low cost processes, and yield dense nanocrystalline deposits under the proper conditions. They are capable of coating large areas for corrosion/thermal protection in aerospace and bio-medical applications (Papyrin et al., 2006). Aerosol deposition is also used on smaller devices like micro-actuators and high-speed optical modulators. Cold spray deposition has received more attention in the literature, and is now an established commercial process for the deposition of ductile metals. Aerosol deposition is at an earlier stage of development, but has been shown to form deposits from finer particle size powders and to form dense ceramic coatings. The cold spray and aerosol deposition methods are merited over other conventional methods, such as physical and

* Corresponding author. Tel.: +82 2 3290 3376; fax: +82 2 926 9290.
E-mail address: skyoon@korea.ac.kr (S.S. Yoon).

chemical vapor deposition (PVD or CVD), because of their ability to cover surface area at rapid deposition rate and at low temperature, which avoids any thermal damage to both coating materials and substrates.

Cold spray and AD deposition systems use *de Laval* convergent–divergent nozzles to accelerate the gas to the required velocities. Computational fluid dynamics (CFD) simulations help to understand the gas flow behavior and to optimize nozzle designs for cold spray systems (Jen et al., 2005; Jodoin, 2002; Nickel et al., 2007; Pattison et al., 2008) and, to a lesser extent, for AD nozzles (Katanoda & Matsuo, 2006). Previous efforts to optimize the nozzle configuration determined that the nozzle exit pressure should equal the ambient pressure ($P_e = P_{amb}$) to achieve a “correctly-expanded” (or shock-free) nozzle (Park et al., 2011). If $P_e > P_{amb}$ or $P_e < P_{amb}$, the nozzle is said to be *under-expanded* or *over-expanded*, respectively, and these are not shock-free (Anderson & David, 1995). When operated at atmospheric pressure, if the nozzle configuration deviates from correctly expanded, it generates an undesirable shear layer, a Mach disk, a reflected compression shock, and an expansion fan, all of which decrease the kinetic energy of the gas flow and adversely affect the overall coating efficiency. When operated at pressures typical of the AD process, the consequences of using a non-correctly-expanded nozzle are generally less severe (Lebedev et al., 2004; Nam et al., 2004). This nozzle optimization process is very well known to the compressible flow community, but has not well been applied to the cold spray and aerosol deposition processes.

This paper examines the design of a nozzle for an AD system operating at an ambient pressure of $P_{amb} = 0.013$ bar using CFD and correlates the performance with experimental observations. The CFD results show significant differences in gas-flow behavior compared to results obtained at $P_{amb} = 1$ bar, typical of cold spray systems. Moreover, the substrate significantly perturbs the flow field in the AD system.

The nozzle is designed to efficiently accelerate titanium dioxide particles through a *de Laval* convergent–divergent nozzle by minimizing shockwave-induced losses (maximizing the kinetic energy of the particles increases the coating efficiency). Titanium dioxide is a common coating material because it has deodorization, bactericidal, and self-cleaning properties (Ryu et al., 2008). It is also used in dye-sensitized solar cells (Fan et al., 2007).

2. Numerical details

The CFD code, *Fluent* 6.3, solves fully compressible Navier–Stokes equations and resolves shockwaves, turbulence, and viscous dissipation effects. Details on the numerical procedures and algorithms used in this code are available in the *Fluent Manual* (Fluent Inc, 2008). The 2D computations are based on second-order-accuracy in the numerical approximations. The nozzle is a 2D slot with an infinite depth. Slot-type nozzles allow relatively large areas to be coated on each pass. An axisymmetric cone nozzle is also used for validation results. A Lagrangian–Eulerian based discrete-phase model is used to track the particles released at the nozzle throat and entrained within the accelerating gas flow, which eventually reach supersonic speeds.

For all computations, 121,600 nodes (i.e., 60×800 for the nozzle and 230×320 for the external domain) are used, with a minimum grid spacing $\Delta x = 0.003$ mm, sufficient to capture the dominant frequency of convective flow as well as the Kolmogorov length scale. Grid sensitivity studies confirmed that the numerical solution is not dependent on the grid resolution when the total number of nodes exceeds about 100,000. No-slip Dirichlet boundary conditions are applied along all the walls, while the Neumann boundary condition is applied at the outlet. The physical size of the computational domain is 50×400 mm. The stagnation pressure is $P_0 = 6$ bar at the nozzle inlet. The working fluid is air at $T_0 = 300$ K. The throat diameter is fixed at $d_t = 0.4$ mm. When the nozzle is operated near vacuum ($P_{amb} = 0.013$ bar), the nozzle exit diameter is $d_e = 10$ mm. When $P_{amb} = 1$ bar, the exit diameter is either under-, correctly-, or over-expanded with exit diameters $d_e = 0.56, 0.70, \text{ or } 1.45$ mm, respectively. The diverging spray angle (θ) changes depending on the exit diameter.

3. Results and discussion

3.1. Validation

Fig. 1 shows the speed contours from the under-, correctly-, and over-expanded nozzles without particles. These simulations demonstrate that the nozzle geometry has a significant effect on the flow inside and outside the nozzle. The nozzle pressure ratios ($NPR = P_0/P_e$, where $P_0 = 6$ bar) are 4.23, 5.77, and 7.83 for the under-, correctly-, and over-expanded cases, respectively; in addition, their respective exit-to-throat area ratios (i.e., $AR = A_e/A_t = (d_e/d_t)^2$ with $d_t = 0.4$ mm) are 1.41^2 , 1.75^2 , and 3.62^2 . Note that NPR is presented as a function of the exit pressure (P_e) instead of the ambient pressure (P_{amb}) to avoid large values of NPR when the ambient pressure nears zero for the case of the vacuum environment. The pattern of alternating low- and high-density regions (diamond shock structures) is observed for the under- and over-expanded nozzles. These structures are most pronounced near the nozzle exit, and they dissipate downstream. Mach disks near the under- and over-expanded nozzle exits contribute to the reduction of flow speeds. Generally, the under-expanded nozzle is prone to swell (see Fig. 1a)—it expands into the surrounding ambient gas because $P_e > P_{amb}$. When $P_e = P_{amb}$ (the correctly expanded case as shown in Fig. 1b), shockwaves are nearly suppressed and flow kinetic energy is maximized.

Fig. 2a and b shows the Schlieren and UV-laser-Rayleigh-scattering images, respectively, of a supersonic non-isobaric and non-isentropic gas jets from an under-expanded nozzle. The pressure ratio is $P_e/P_{amb} = 2.3$ for the Schlieren image from Zapryagaev et al. (2002) in Fig. 2a. The UV-laser-Rayleigh-scattering images from Dam et al. (1998) in Fig. 2b shows how four periodic diamond structures form within 26 mm downstream; the white rectangle is the nozzle exit.

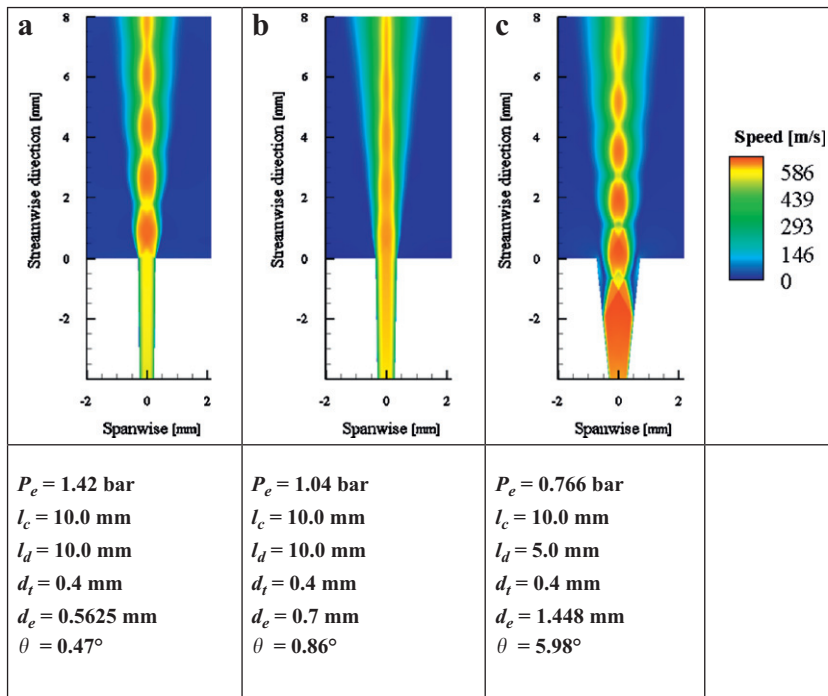


Fig. 1. Effects of nozzle geometry on supersonic flow characteristics when $P_{amb}=1$ bar. The nozzle exit is located at $x=0$ mm: (a) under-expanded, (b) correctly-expanded and (c) over-expanded.

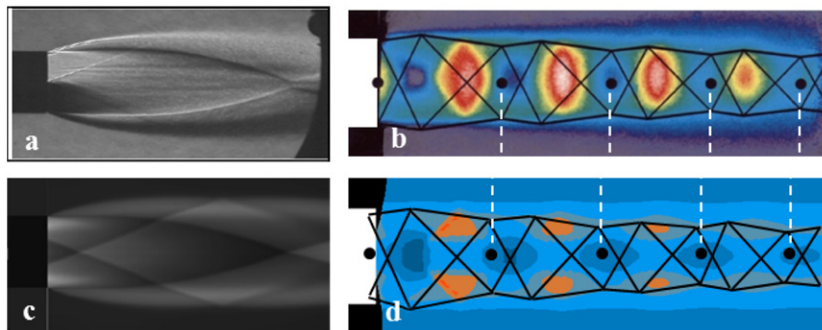


Fig. 2. Qualitative comparisons between experiments and our simulations of a supersonic, non-isobaric gas jet for the under-expanded nozzle. (a) Details for the Zapryagaev et al. (2002) nozzle: a conical nozzle with a 15° half-angle at $M=3$. The nozzle exit inner and outer diameters are 30 and 32 mm, respectively. The nozzle exit pressure is $n=P_e/P_{amb}=2.3$. (b) Generation of diamond shockwaves exiting from Dam et al.'s (1998) under-expanded nozzle. The snapshot is taken on the time scale of the duration of the laser pulse (18 ns). The nozzle stagnation pressure is 3 bar. Lines indicate shock and expansion waves while dots represent the density maxima.

Our axisymmetric model of the Dam et al. experiment in Fig. 2d correctly approximates the frequency of the *four* diamond shockwaves. The diamond shockwaves dissipate downstream both in the experimental image and in our simulation. Moreover, the model correctly predicts the expansion of the jet downstream. It should be noted that Fig. 2c and d are obtained on the basis of the axisymmetric (i.e., $z-r$ axes) simulations while all other computational runs are based on the 2D (i.e., $x-y$) model.

For an additional validation data, Fig. 3 compares our computational results against those of Nickel et al. (2007), which was simulated with $P_0=120$ bar and $T_0=1800$ K. A single copper particle (whose diameter is $D_p=15$ μm) was released at the streamwise location of $x_{inj}=0.05$ and 0.1 m and the particle speed is tracked and recorded. The two different particle-injection locations were set with the intention of investigation different thermal load on particle, depending on x_{inj} . Note that the nozzle throat, whose diameter is $d_t=7.9$ mm, is located at origin ($x=0$). The nozzle length extends up to $l_c+l_d=0.356$ m. The particle speed was initially set to 15 m/s and is gradually accelerated up to the speed of greater than 1000 m/s at the nozzle exit. Our results slightly differs from those obtained by Nickel et al. (2007). These differences in results are attributed to the differences in numerical approaches, such as order of scheme, shock treatment, and turbulence model. Because these numerical approaches are not detailed in Nickel et al. (2007), the result differences were not

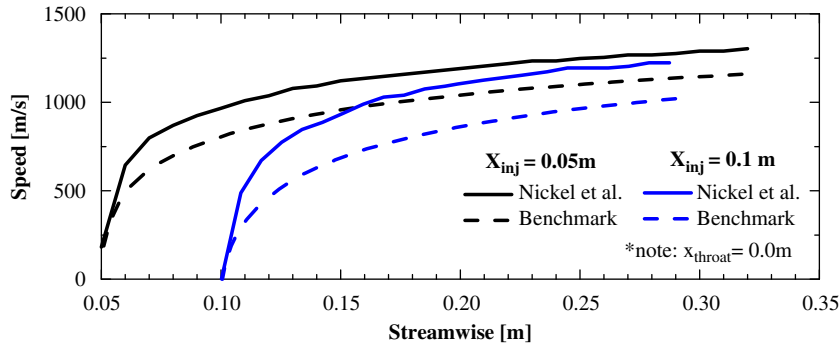


Fig. 3. Comparison between our computational results (dashed lines) and those by Nickel et al. (2007) (solid line). The nozzle throat is at $x=0$ m. Two computational runs are shown: A copper sphere is released at $x_{inj}=0.05$ and 0.1 m.

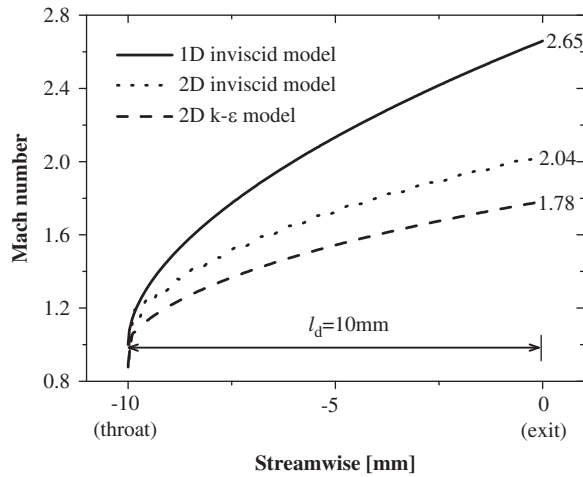


Fig. 4. The effect of dimensionality and viscosity on the Mach number. The effect of dimensionality change (going from 1D to 2D) causes 23% reduction in the Mach number for the correctly expanded case. Adding viscosity yields an additional 13% Mach number reduction (2.04–1.78).

inexorable. Nevertheless, the overall results are well compared, though there are some slight differences in the magnitude of the particle speed.

3.2. Simulations

For a 1D isentropic flow (inviscid and adiabatic), the Mach number as a function of axial distance is found by combining the isentropic relations with the continuity equation:

$$\frac{A_e}{A_t} = \left(\frac{1}{M_e}\right) \left[\left(\frac{2}{\gamma+1}\right) \left(1 + \frac{\gamma-1}{2} M_e^2\right) \right]^{(\gamma+1)/2(\gamma-1)} \quad (1)$$

Our CFD simulations solve the nonlinear, 2D viscous Navier–Stokes equations. By comparing the results of these CFD simulations to the analytical, 1D inviscid flow solution, the change in dimensionality (1D to 2D) and the viscous effects are quantified as shown in Fig. 4 where the correctly expanded case of Fig. 1 is considered. The throat where the Mach number is unity (based on 1D inviscid flow) is at $x = -10$ mm and the exit is at the origin, $x = 0$ mm. The Mach number increases through the diverging nozzle (supersonic expansion) as the initial stagnation pressure is converted into kinetic energy. Comparing the Mach numbers at the exit, the effect of dimensionality change (going from 1D to 2D) causes 23% reduction in the Mach number for the correctly expanded case. Adding viscosity yields a 13% reduction of Mach number from 2.04 to 1.78. Obviously, it is seen that dimensionality increase has a bigger impact on Mach number than viscosity (for this gas).

To find the impact speed of the coating materials, aluminum, titanium, and steel particles of various sizes and densities are released at the nozzle throat and their trajectories are recorded until they reach steady-state velocity. Note that the nozzle used herein is the correctly-expanded nozzle. For efficient coating, the coating substrate should be distanced from the nozzle to allow the particles to reach maximum velocity at the instant of impact. Particle impact speed as a function of the Stokes number is shown in Fig. 5. The Stokes number is defined as $Stk = \tau_p / \tau_g$, where $\tau_p = \rho_p D^2 / (18 \mu_g)$ is the particle response time to the surrounding flow and $\tau_g = d / u_{g,exit}$ is the characteristic time of the surrounding flow; ρ_p and D are the

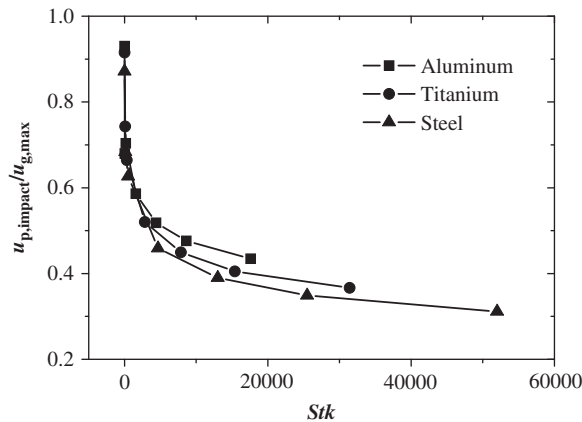


Fig. 5. Normalized particle speed as a function of Stokes number.

particle density and diameter, respectively; μ_g is the gas dynamic viscosity, and d and $u_{g, \text{exit}}$ are the nozzle exit diameter and gas speed, respectively. If $\tau_p \ll \tau_g$ (or $Stk \ll 1$), the particles are quick to respond to the flow. Conversely, if $\tau_p \gg \tau_g$ (or $Stk \gg 1$), the particles are slow to respond to the flow and not easily accelerated. Fig. 5 confirms this trend. With decreasing Stokes number, particles approach the speed of the surrounding gas. Note that the particle impact speeds differ by 5–10% while their densities differ more significantly: $\rho_{\text{Al}}=2719$, $\rho_{\text{Ti}}=4850$, and $\rho_{\text{Fe}}=8030 \text{ kg/m}^3$ (even at the same Stokes number).

Nozzle optimization is crucial to minimizing shock loss. When the surrounding ambient pressure changes from $P_{\text{amb}}=1$ to 0.013 bar (i.e., nearly a vacuum), the nozzle geometry should be changed such that the pressure at the nozzle exit is also $P_e=0.013$ bar, which is equal to P_{amb} . The exit area (or diameter) of the nozzle that yields the shock-free (or correctly-expanded) condition of $P_e=P_{\text{amb}}$ can be estimated by using the 1D-isentropic solution. For example, for $P_e=P_{\text{amb}}$, the exit Mach number can be estimated with the isentropic relationship $P_0/P_{\text{amb}}=(1+0.2M_e^2)^{3.5}$, which can be substituted into Eq. (1) to calculate the optimal geometry, A_e . Conversely, this implies that if A_e is fixed, then M_e is also fixed. Because this estimate is based on a 1D-inviscid analysis, it could have up to 33% error (see Fig. 4). Real supersonic flows (2D or 3D viscous flow) are sensitive to exit pressure and cannot afford such inaccuracies; even at an exit pressure of $P_e=1.04$ bar (4% different from $P_{\text{amb}}=1$ bar), small shockwaves are evident (Fig. 1b).

Fig. 6 compares the speed results obtained from CFD computation for two nozzles at the near-vacuum condition of $P_{\text{amb}}=0.013$ bar. The *first* nozzle geometry has throat and exit diameters of $d_t=0.4$ and $d_e=10$ mm, respectively, and the diverging nozzle length (throat to exit) is $l_d=30$ mm. The *second* nozzle has throat and exit diameters of $d_t=1.3$ and $d_e=1.56$ mm, respectively, and the diverging nozzle length (throat to exit) is $l_d=15$ mm. For comparison purposes, the *first* nozzle in the left column is correctly expanded while the *second* nozzle in the right column is under-expanded.

In Fig. 6, the CFD results are obtained for two different scenarios: one without a substrate (figures in the first row) and other with a substrate (figures in the second row). Having the substrate in the flow path affects upstream flow; compare the figures in the first and second rows in Fig. 6. The high-speed region in flow center is significantly narrowed by the infiltration of the low-speed region toward the nozzle edge. Other potential problem includes shockwaves traveling upstream and undermining the performance of the nozzle if the substrate is too close to the nozzle exit.

3.3. Experiment

Fig. 7 shows the schematic of our experimental setup for the aerosol deposition system. The vacuum and booster pumps are attached to the chamber, which keeps the chamber at low pressure. The working fluid (i.e., air or inert gases) is injected the powder feed and then eventually is accelerated through the converging and diverging with TiO_2 particles. TiO_2 powder is pre-mixed with dry-air in a suspension cylinder and fed into the nozzle, which accelerates the TiO_2 particles to supersonic speeds. The mass flowrate of the supplied air is 7 l/min. The averaged particle size is $d_{50}=3 \mu\text{m}$; thus, $Stk < 0.2$, which implies that the particles attain more than 90% of the maximum speed of the gas flow (see Fig. 5). The substrate is situated about 15 mm away from the nozzle. A 2D, slot-type nozzle is installed onto a maneuvering stage that moves at 1 mm/s; thus, it requires about 50 s to traverse the 5 cm-long substrate. The nozzle coats the substrate 3 times to form multiple layers to a total thickness of up to 3 μm (approximately 1 μm per pass). While a uniform distribution of the injected powder is desired across the nozzle exit, it is possible that particle number density at the nozzle center is greater than that at the periphery of the spray (potentially giving a parabolic distribution). Overall, the primary parameters impacting coating efficiency are (1) nozzle geometry, (2) particle size and mass flowrate, (3) air mass flowrate, and (4) nozzle–substrate distance.

Upon high-speed impact of a particle onto the substrate, the particle disintegrates into nano-sized sub-grains whose sizes can be approximated through recrystallization theory (Humphreys & Hatherly, 2004). Because of the high impact speeds, pressure builds up at the impact point to up to tens of GPa (Kim et al., 2008). Shear stress between the impacting

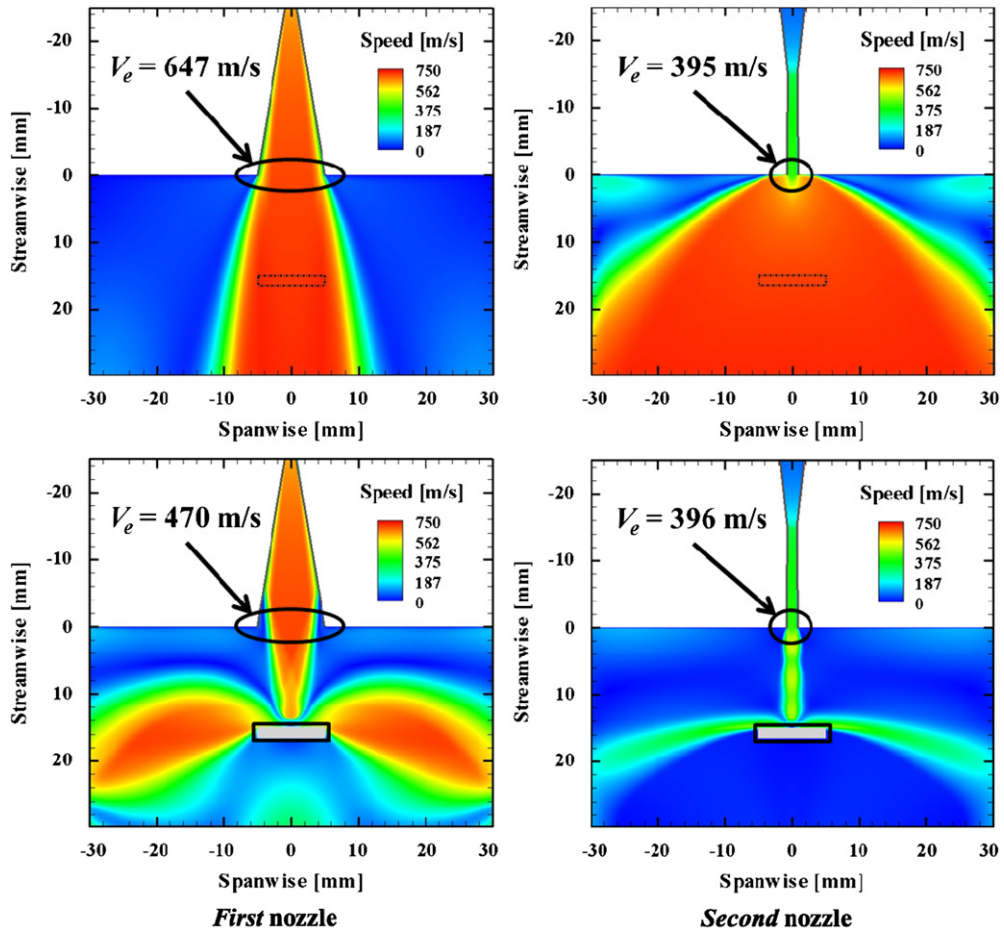


Fig. 6. CFD predictions of the gas speed for the two nozzles: the *first* nozzle is correctly expanded, while the *second* nozzle is under-expanded. The *first* nozzle geometry has throat and exit diameters of $d_t=0.4$ and $d_e=10$ mm, respectively, and the diverging nozzle length (throat to exit) is $l_d=30$ mm. The *second* nozzle has throat and exit diameters of $d_t=1.3$ and $d_e=1.56$ mm, respectively, and the diverging nozzle length (throat to exit) is $l_d=15$ mm. The snapshots in the first and second row represent the CFD results *without* and *with* the substrate, respectively.

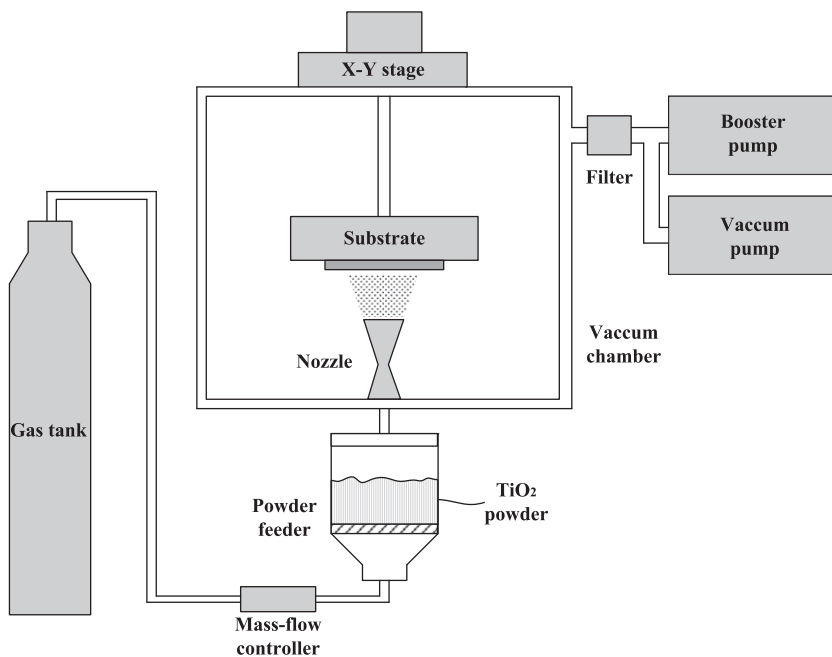


Fig. 7. Schematic of the experimental setup for the aerosol deposition system.

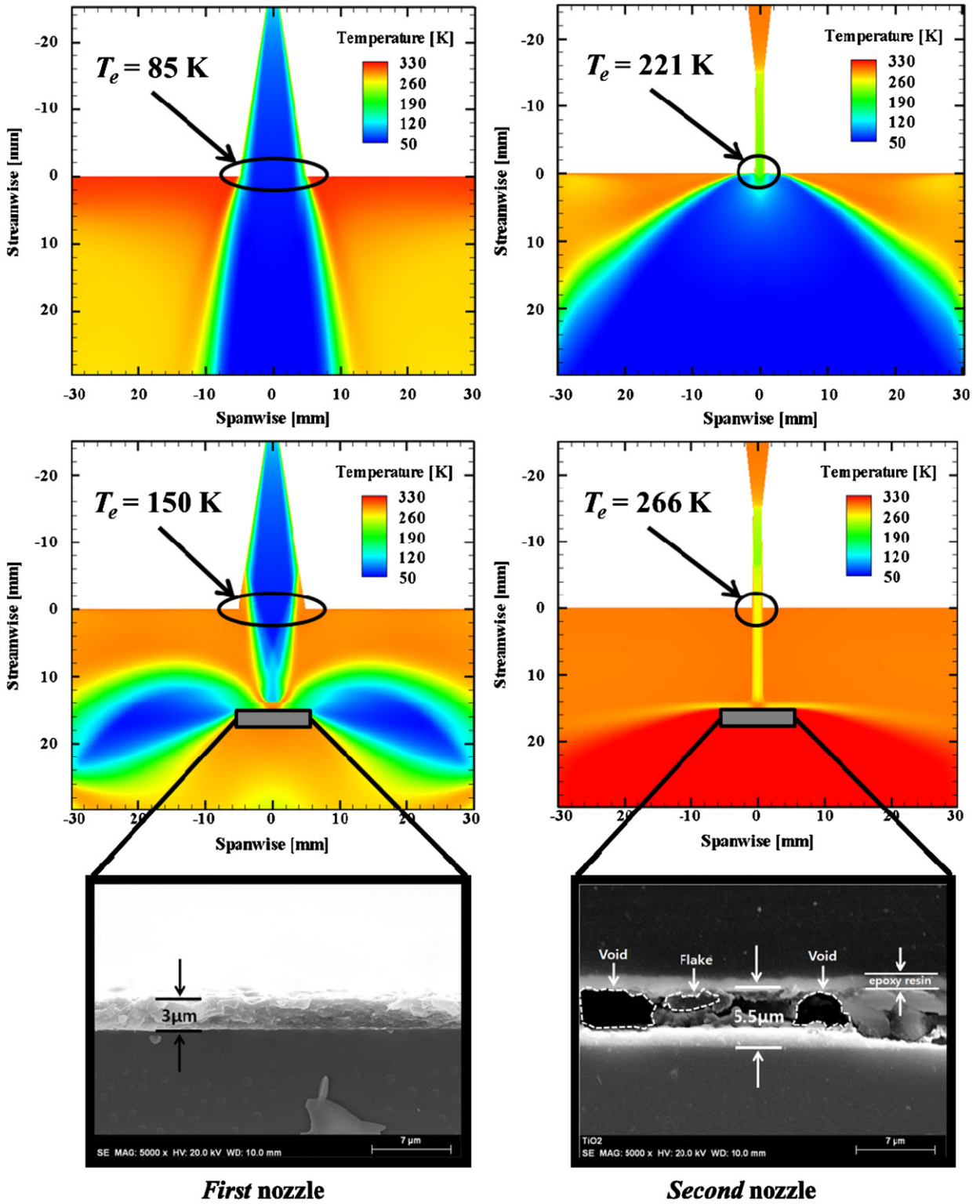


Fig. 8. CFD predictions on gas temperature and their application to actual coating of TiO_2 powder. These figures compare the CFD and experimental results of two nozzles in conjunction with Fig. 6.

particle and substrate yields jetting fingers at the periphery of the particle (Kim et al., 2008). However, dislocated subgrains quickly adhere to the substrate before re-solidification. For successful bonding of a solid particle to a substrate, the particle must exceed a critical velocity, which is a function of the thermo-mechanical properties of the spray and also the

substrate material (Assadi et al., 2003). Below the critical velocity, impacting particles could damage the substrate (foreign object damage) (Nicholls et al., 1997).

Because the particle velocity is always less than the gas velocity (see Fig. 5), the gas velocity must be well over the critical velocity to achieve high-quality coating. Based on our CFD computations, we designed a correctly expanded nozzle that maximizes gas kinetic energy. When a nozzle is poorly designed, particles are not efficiently accelerated, and, thus, they may adhere poorly.

To elucidate our point, we designed two nozzles and compared their coating performances. The *first* nozzle is correctly expanded or designed, (i.e., $P_e = P_{amb}$) and the *second* is under-expanded ($P_e > P_{amb}$). The physical dimensions of the *first* and *second* nozzles are listed in Fig. 6. The isentropic relation of Eq. (1) suggests an exit gas velocity of 440 m/s. Because the isentropic relation assumes frictionless flow, the actual velocity is less; the 2D *Fluent* simulation that includes viscous effects indicates an exit velocity of 390 m/s. Furthermore, we expect degraded coating performance from the *second* nozzle because particle impact velocity is well below its critical velocity,

As expected, the experimental scanning electron microscopy (SEM JSM-5800, JEOL, Japan) images shown in Fig. 8 (last row) confirmed our expectation. The 3 μm -thick TiO_2 layer from the *first* nozzle is dense and free of voids (bottom-left in Fig. 8). The layer obtained using the *second* nozzle shows voids and irregularity; Fig. 8 (bottom-right). SEM images were obtained by cutting the coated substrate in half. The well-coated substrate was easily cut while the poorly coated substrate needed epoxy-resin protection because of poor adhesion of particles onto the substrate surface. This epoxy-resin is the light region on top of the “flakes” and “voids” shown in Fig. 8 (bottom-right). Top views of the well- and poorly coated substrates also show distinctive differences in uniformity and quality (now shown here for brevity) with the well-coated substrate having a relatively smooth surface and the poorly coated one with significant irregularity.

The overall temperature distribution from the computational results for these two nozzles is also shown in Fig. 8. This temperature distribution explains the velocity difference between the two nozzles. From the second rows in Fig. 8, the *first* nozzle efficiently converts all available stagnation pressure and temperature into kinetic energy, which in turn yields a low temperature region through the nozzle. Contrastively, the *second* nozzle suffers from converting thermal energy into kinetic energy; the temperature distribution is relatively high at the nozzle exit. One may additionally compare the computational results for the case *with* and *without* the substrate from Fig. 8. Behind the nozzle exit, gas is successively accelerated for both *first* and *second* nozzle case when there is no substrate. The vacuum condition of the chamber permits this efficient flow acceleration regardless of the nozzle shape. However, when the substrate is present, the flow is stagnated and the nozzle optimization plays a significant role in flow acceleration.

Fig. 9 shows the density distribution of the gas for the two nozzle cases. It should be noted that the density contour for the results shown for the *first* and *second* nozzles is at different level for the purpose of clear presentation. As mentioned

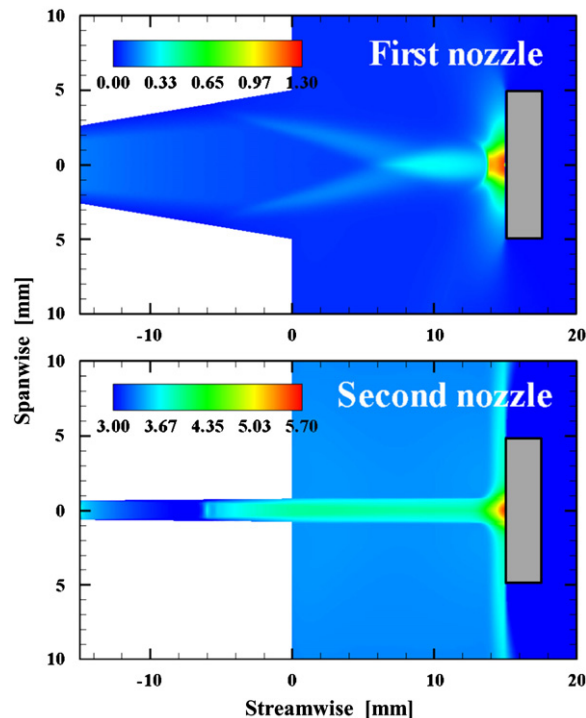


Fig. 9. Density distribution of the gas. A bow shock is formed for the *first* nozzle case because the flow is supersonic. As for the *second* nozzle case, gas densification is prominent in the streamline because of relatively low-speed flow.

earlier, the *first* nozzle efficiently accelerates the gas that enables yielding a supersonic flow, in which case the shock wave may be formed. As shown, a minor oblique shock is formed for the *first* nozzle, which is a proof of its supersonic state though, strictly speaking, the shock itself is not desirable. It should be noted that a complete removal of shock formation is extremely difficult, especially when there is a substrate because it bounces the pressure disturbance toward all directions. As for the *second* nozzle, the flow is not supersonic because the nozzle is not optimized. Because the gas has not been efficiently accelerated, gas molecules are accumulated inside the streamline, resulting in densification of the streamline, as shown in Fig. 9. There is no evidence of shock for the subsonic *second* nozzle case while, for the *first* nozzle case, shocks are found near the nozzle exit (i.e., oblique shock) and the substrate (i.e., bow shock). Across the bow shock, gas densification is obviously present, which in turn increases drag on particles, thereby slowing them (Pattison et al., 2008). As the particle's final impact velocity controls the coating efficiency, the appearance of a bow shock right before the substrate is an issue for particle deposition processes. Care should be taken not to use particles that are too small to minimize the effects in the bow shock region that could prevent particles from adhering onto the substrate.

4. Conclusion

This paper characterizes the performance of supersonic nozzle flows, both numerically and experimentally. Effects of shockwaves, nozzle geometry and dimensionality, carrier-gas viscosity, and particle density have been studied computationally. Nozzle optimization is required because shockwave-induced fluctuations can yield non-uniform coating. Nozzle geometry was adjusted to yield the optimum condition of $P_e = P_{amb}$, which significantly reduced shock formation and maximized kinetic energy. Reducing the chamber pressure from $P_{amb} = 1$ to 0.01316 bar necessitated a nozzle with a greater diverging angle than the nozzle previously used to maintain optimal coating performance. Based on the computational results, two nozzles were designed experimentally. The *first* nozzle, optimally designed ($P_e = P_{amb}$), yielded a dense and void-free coating layer while the *second* nozzle (non-optimized, under-expanded, $P_e > P_{amb}$) yielded voids and irregularity.

Acknowledgment

This work was supported by the New & Renewable Energy Program through a grant by the Korea Institute of Energy Technology Evaluation and Planning (KETEP, 2010–3010010011) and the Fundamental R&D Program for Core Technology of Materials funded by the Ministry of Knowledge Economy of Korea. This work was also supported by the Center for Inorganic Photovoltaic Materials (NRF-2011-0007182), (NRF-2010-D00013), and the Converging Research Center Program through the Ministry of Education, Science and Technology (2010K000969).

References

- Akedo, J. (2006). Aerosol deposition of ceramic thick films at room temperature: densification mechanism of ceramic layers. *Journal of the American Ceramic Society*, 89, 1834–1839.
- Anderson, J.D., & David, J. (1995). *Computational Fluid Dynamics*. McGraw-Hill: New York.
- Assadi, H., Gartner, F., Stoltenhoff, T., & Kreye, H. (2003). Bonding mechanism in cold gas spraying. *Acta Materialia*, 51, 4379–4394.
- Blais, A., Jodoin, B., Dorier, J.L., Gindrat, M., & Hollenstein, C. (2005). Inclusion of aerodynamic non-equilibrium effects in supersonic plasma jet enthalpy probe measurements. *Journal of Thermal Spray Technology*, 14, 342–353.
- Chun, D.M., & Ahn, S.H. (2011). Deposition mechanism of dry sprayed ceramic particles at room temperature using a nano-particle deposition system. *Acta Materialia*, 59, 2693–2703.
- Dam, N.J., Rodenburg, M., Tolboom, R.A.L., Stoffels, G.G.M., Huisman-Kleinherenbrink, P.M., & ter Meulen, J.J. (1998). Imaging of an underexpanded nozzle flow by UV laser Rayleigh scattering. *Experiments in Fluids*, 24, 93–101.
- Fan, S.Q., Li, G.J., Yang, G.J., Zhang, L.Z., Gao, J.C., & Xi, Y.X. (2007). Fabrication of nano-TiO₂ coating for dye-sensitized solar cell by vacuum cold spraying at room temperature. *Journal of Thermal Spray Technology*, 16, 893–897.
- Fan, S.Q., Yang, G.J., Li, C.J., Liu, C.J., & Zhang, L.Z. (2006). Characterization of microstructure of nano-TiO₂ coating deposited by vacuum cold spraying. *Journal of Thermal Spray Technology*, 15, 513–517.
- Gartner, F., Stoltenhoff, T., Schmidt, T., & Kreye, H. (2006). The cold spray process and its potential for industrial applications. *Journal of Thermal Spray Technology*, 15, 223–232.
- Fluent Inc. (2008). *Fluent User's Guide*.
- Humphreys, F.J., & Hatherly, M. (2004). *Recrystallization and Related Annealing Phenomena*. Elsevier: Amsterdam.
- Jen, T.-C., Li, L., Cui, W., Chen, Q., & Zhang, X. (2005). Numerical investigations on cold gas dynamic spray process with nano- and microsize particles. *International Journal of Heat and Mass Transfer*, 48, 4384–4396.
- Jodoin, B. (2002). Cold spray nozzle Mach number limitation. *Journal of Thermal Spray Technology*, 11, 496–507.
- Karimi, M., Fartaj, A., Randin, G., Vanderzwet, D., Birtch, W., & Villafuerte, J. (2006). Numerical simulation of the cold gas dynamic spray process. *Journal of Thermal Spray Technology*, 15, 518–523.
- Katanoda, H., Fukuhara, M., & Ino, N. (2007). Numerical study of combination parameters for particle impact velocity and temperature in cold spray. *Journal of Thermal Spray Technology*, 16, 627–633.
- Katanoda, H., & Matsuo, K. (2006). Gasdynamic simulation of aerosol deposition method. *Materials Transactions*, 47, 1620–1625.
- Kim, K.H., Watanabe, M., Kawakita, J., & Kuroda, S. (2008). Grain refinement in a single titanium powder particle impacted at high velocity. *Scripta Materialia*, 59, 768–771.
- Lebedev, M., Akedo, J., & Itawa, A. (2004). NiZnCu ferrite thick film with nano scale crystallites formed by the aerosol deposition method. *Journal of the American Ceramic Society*, 87, 1621–1624.
- Li, W.Y., & Li, C.J. (2005). Optimal design of a novel cold spray gun nozzle at a limited space. *Journal of Thermal Spray Technology*, 14, 391–396.
- Li, W.Y., Liao, H., Douchy, G., & Coddet, C. (2007). Optimal design of a cold spray nozzle by numerical analysis of particle velocity and experimental validation with 316L stainless steel powder. *Materials and Design*, 28, 2129–2137.

- Li, W.Y., Liu, C.-J., Wang, C.X., & Bang, H.S. (2006). Measurement and numerical simulation of particle velocity in cold spraying. *Journal of Thermal Spray Technology*, 15, 559–562.
- Nam, S.M., Naoko, M., Hirofumi, K., Satoshi, W., Akedo, J., & Tsurumi, T. (2004). Alumina thick films as integral substrates using aerosol deposition method. *Japanese Journal of Applied Physics*, 43, 5414–5418.
- Nicholls, J.R., Jaslier, Y., & Rickerby, D.S. (1997). Erosion and foreign object damage of thermal barrier coatings. *Material Science Forum*, 251–254, 935–948.
- Nickel, R., Bobzin, K., Lugscheider, E., Parkot, D., Varava, W., & Oliver, H. (2007). Numerical studies of the application of shock tube technology for cold gas dynamic spray process. *Journal of Thermal Spray Technology*, 16, 729–735.
- Papyrin, A., Kosarev, V., Klinkov, K.V., Alkhimov, A., & Fomin, V.M. (2006). *Cold Spray Technology*. Elsevier: Oxford, U.K.
- Park, J.J., Lee, M.W., Yoon, S.S., Kim, H.Y., James, S.C., Heister, S.D., Chandra, S., Yoon, W.H., Park, D.S., & Ryu, J. (2011). Supersonic nozzle flow simulations for particle coating applications: effects of shockwaves, nozzle geometry, ambient pressure, and substrate location upon flow characteristics. *Journal of Thermal Spray Technology*, 20, 514–522.
- Pattison, J., Celotto, S., Khan, A., & O'Neil, W. (2008). Standoff distance and bow shock phenomena in the Cold Spray process. *Surface and Coatings Technology*, 202, 1443–1454.
- Raletz, F., Vardelle, M., & Ezo'o, G. (2006). Critical particle velocity under cold spray conditions. *Surface and Coatings Technology*, 201, 1942–1947.
- Ryu, J.H., Park, D.S., Hahn, B.D., Choi, J.J., Yoon, W.H., & Kim, K.Y. (2008). Photocatalytic TiO₂ thin films by aerosol-deposition: from micron-sized particles to nano-grained thin film at room temperature. *Applied Catalysis B*, 83, 1–7.
- Zahiri, S.H., Yang, W., & Jahedi, M. (2009). Characterization of cold spray titanium supersonic jet. *Journal of Thermal Spray Technology*, 18, 110–117.
- Zapryagaev, V.I., Kudryavsev, A.N., Lokotok, A.V., Solotchin, A.V., Pavlov, A.A., & Hadjadj, A. (2002). An experimental and numerical study of a supersonic-jet-shock-wave structure. In: Proceedings of the XI International Conference on the Methods of Aerophysical Research, Vol. 2, pp. 187–191.